Size controlled CuO nanoparticles for Li-ion batteries

Oliver Waser [a], Michael Hess [b], Andreas Güntner [a], Petr Novák [b], Sotiris E. Pratsinis [a],*

[a] Particle Technology Laboratory, Department of Mechanical and Process Engineering, ETH Zurich, Sonneggstrasse 3, CH-8092 Zurich, Switzerland
[b] Electrochemistry Laboratory, Department of General Energy, Paul Scherrer Institute, CH-5232 Villigen PSI, Switzerland

HIGHLIGHTS

- Size controlled & scalable synthesis of CuO nanoparticles from 6 to 50 nm (d_{BET}).
- Theoretical specific charge of 674 mA h g^{-1} achieved for 20 nm CuO particles.
- Enhanced oxidation/reduction of nano-sized CuO particles proven by XANES and XRD.

GRAPHICAL ABSTRACT
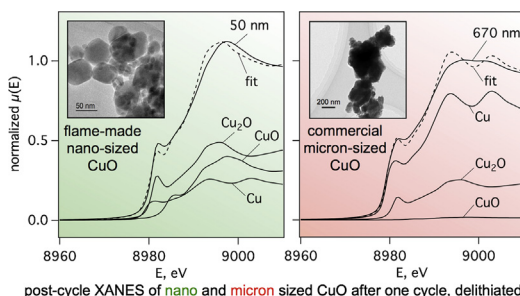
post-cycle XANES of nano and micron sized CuO after one cycle, delithiated

ARTICLE INFO

ABSTRACT

Monocrystalline copper(II) oxide nanoparticles were made by scalable flame spray pyrolysis (FSP) and analyzed by X-ray diffraction (XRD), nitrogen adsorption (BET), transmission electron microscopy (TEM) and X-ray absorption near edge structure (XANES). Their primary particle diameter was closely controlled from 6 to 50 nm by varying the FSP conditions. Their electrochemical performance as Li-ion battery materials was tested in composite electrodes vs. Li-metal. Near theoretical specific charges were obtained for intermediate CuO sizes of 20 and 50 nm (d_{BET}). In contrast, larger, commercially available CuO ($d_{BET} = 670$ nm) exhibited significantly lower practical specific charge due to incomplete oxidation in the delithiation cycle as indicated by the remaining Cu and Cu_2O by XRD and XANES analysis.

1. Introduction

Classic Li-ion batteries use mostly insertion-type cathode materials containing transition-metal oxides such as $LiCoO_2$ [1] and their more recent substitutes $LiMn_2O_4$ and $LiCo_{1/3}Ni_{1/3}Mn_{1/3}O_2$ [2,3] or transition-metal phosphates like $LiFePO_4$ [4]. These

substitutes lead to lower cost, enhanced performance and improved safety [5]. Nevertheless, insertion-type materials typically show an intrinsic barrier toward higher specific charges as the available Li-sites in the host lattice are limited [6]. In addition, the allowed number of exchanged Li-ions is often restricted due to the onset of irreversible crystal structure alterations [7]. A breakthrough in specific energy necessitates a novel concept of Li-ion storage materials [5].

Systems based on conversion-type materials [8] offer higher specific energy than those using insertion materials since Li directly undergoes an electrochemical reaction with the transition-metal compound, allowing full utilization of its charge states [9].

* Corresponding author. ETH Zurich, ML F13.1, Sonneggstrasse 3, CH-8092 Zürich, Switzerland. Tel.: +41 44 632 31 80; fax: +41 44 632 15 95.
  E-mail addresses: pratsinis@ptl.mavt.ethz.ch, sotiris.pratsinis@ptl.mavt.ethz.ch (S.E. Pratsinis).

Various transition metals (e.g. Ti, V, Cr, Mn, Fe, Co, Ni, Cu, Mo, W and Ru) combined with anions (e.g. O, N, F, S, P and even H) yield electrochemically-active compounds [5]. Their drawback, however, is a rather high potential hysteresis between charge and discharge, resulting in reduced energy efficiency [10] and rather limited cycling stability [11].

Copper oxide is an attractive conversion (active) material as it is inexpensive, relatively non-toxic, and has about twice the theoretical specific charge (674 mA h g^{-1}) of the widely used graphite anode (372 mA h g^{-1}) [12]. Due to the reasonably high conversion voltage of CuO (for conversion reactions), it can be readily used as cathode material, offering a theoretical specific energy (with respect to the oxide only and assuming a negative electrode with $E = 0$ V vs. Li$^+$/Li) of about 944 Wh kg^{-1} (674 mA h g^{-1} at 1.4 V vs. Li$^+$/Li) corresponding to 164% of the practical value for the commonly used LiCoO$_2$ with 576 Wh kg^{-1} (160 mA h g^{-1} @ 3.6 V). CuO also shows promising cycle life for sub-micrometer particles [13], fast cycling rates [12] and, most interestingly, high specific charge for nanostructured electrodes [14].

Though CuO can be made by dry or wet chemistry processes, the former are quite attractive for their scalability, simplicity, ease of particle collection and high product purity [15]. Among them, flame spray pyrolysis (FSP) is a versatile technique for synthesis of active materials (LiMn$_2$O$_4$, Li$_4$Ti$_5$O$_{12}$, LiFe$_5$O$_8$) for batteries [16]. Furthermore, material synthesis by FSP can be combined with acetylene-black (ACB) formation to result in battery electrodes (e.g. LiMn$_2$O$_4$) with improved cycling rate [17]. Most recently, LiFePO$_4$ nanoparticles were made by FSP and in-situ coated with a nanothin acetylene carbon black layer [18]. Electrodes made with such materials exhibited enhanced rate and cycle stability compared to commercial LiFePO$_4$. Characteristically for flame-made nanoparticles, the primary-particle size can be controlled easily [19], offering ideal conditions for size-effect analysis [20].

Here, CuO nanoparticles of closely controlled average diameter from 6 to 50 nm are made by FSP. The influence of FSP conditions is investigated with respect to product crystal size or primary particle diameter and phase composition. That way, the size-specific electrochemical performance of nano CuO is explored and compared to that of commercially available sub-micron sized CuO.

2. Experimental

2.1. Particle synthesis

Nano-sized CuO particles were made by FSP in an open [21] or tube-enclosed [22] burner. Fig. 1 shows a schematic of the enclosed FSP configuration where a quartz glass tube of 4.7 cm inner diameter, 0.25 cm wall thickness and 20 cm length serves as enclosure (the tube is removed for standard, open FSP configuration). The precursor solution (0.25 or 0.5 M Cu) consisted of Soligen Copper 8 (OMG Borchers GmbH, 8.04 wt. % Cu) diluted with a 2:1 (by volume) mixture of 2-ethylhexanoic acid (2-EAH, Sigma Aldrich, >99%) and Xylene (Sigma Aldrich). This solution is fed into the FSP burner at $P = 2-7$ mL min^{-1} and dispersed into a spray by O$_2$ (PanGas > 99.95%) at $D = 4-8$ L min^{-1} at constant pressure drop of 1.8 bar(g). The P/D ratio describes the FSP synthesis conditions here. The spray was ignited and supported by a stoichiometrically premixed flame of 1.25 L min^{-1} CH$_4$ (PanGas > 99.5%) and 2.5 L min^{-1} O$_2$. A sheath gas stream of 10 L min^{-1} O$_2$ was introduced through 32 holes ($\phi = 0.6$ mm) surrounding the nozzle to ensure full oxidation of the precursor [23]. The dry and ready-to-use CuO particles were produced at maximal 17 g h^{-1} and collected on glass-fiber filters (ALBET GF6, 25.7 cm in diameter) with the aid of a vacuum pump (Busch Mink MM 1324AV).
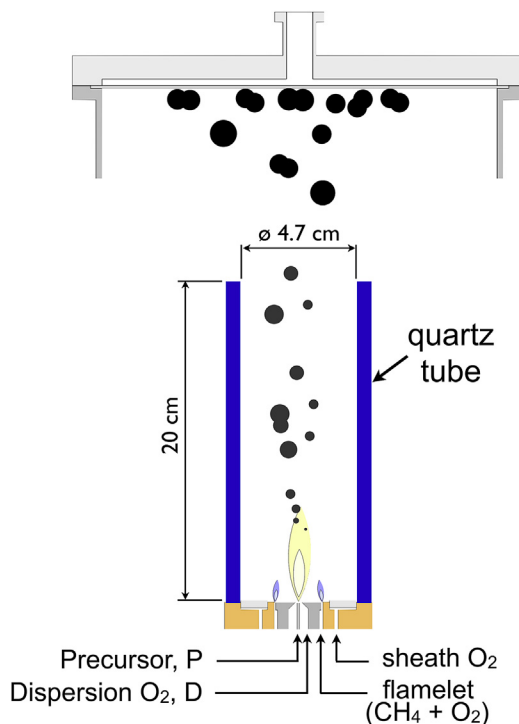

Fig. 1. Schematic of flame spray pyrolysis (FSP) unit for synthesis of CuO nanoparticles of various sizes. For open FSP operation, the quartz-glass tube was removed.

2.2. Particle characterization

Product powders were characterized by N$_2$ adsorption (5-point isotherm for specific surface area, SSA), powder X-ray diffraction (XRD), and transmission electron microscopy (TEM). Powder XRD scans were conducted with a Bruker AXS D8 Advance equipped with a LynxEye 1-dimensional detector and Cu-Kα radiation ($\lambda = 0.154$ nm). Data analysis was conducted with Bruker AXS Topas 4.2 software.

As a measure of CuO size, the Brunauer–Emmett–Teller equivalent diameter is used: $d_{BET} = 6/(SSA^* \rho_{CuO})$, with a CuO (Tenoride) density of $\rho_{CuO} = 6.52$ g cm^{-3}. Sample electrodes (free-standing electrodes) were also analyzed by X-ray diffraction and X-ray absorption near edge structure (XANES) with the SuperXAS-Beamline at Swiss Light Source (SLS) after electrochemical cycling. These electrodes were extracted from the test cells in an argon-filled glove box (<1 ppm O$_2$, N$_2$ and H$_2$O) and encapsulated in Kapton foil prior to its analysis. The oxidation state of Cu was determined from fitting of the XANES spectra with Athena software [24] using three reference spectra (CuO, Cu$_2$O and metallic Cu, recorded in the same XANES session) in the energy range of 25 eV before and after the Cu K-edge.

2.3. Electrochemical characterization

Electrode material slurries were prepared by dispersing 70 wt% active CuO, 10 wt% acetylene carbon black (TIMCAL SuperP) and 20 wt% polyvinyldiene fluoride (PVDF, SOLEF 1015 Solvay) in acetone. Test electrodes were prepared by doctor-blading the slurries on a PTFE surface at a "wet" thickness of 250 μm and drying them at room temperature for 3 min. The dry film was peeled-off from the PTFE and punched into disc electrodes of 1.3 cm in diameter. The free-standing electrodes were dried for 12 h at 120 °C in vacuum and built into coin-type test cells [25] in an argon-filled glove box (<1 ppm O$_2$, N$_2$ and H$_2$O). Lithium metal (99.9%, Sigma

Aldrich) served as counter and reference electrode and 1 M $LiPF_6$ dissolved in ethylene carbonate (EC) and dimethyl carbonate (DMC) 1:1 (by weight) was used as electrolyte [13]. The cells were analyzed by galvanostatic cycling at C/5 or C/10 rate (1 C = 674 mA g^{-1} of active material, CuO) between 0.01 and 3 V vs. Li^+/Li with potentiostatic steps after charge and discharge until the current dropped to C/50. All electrochemical measurements were performed at 25 ± 0.1 °C in an environmental chamber. Error bars generally show the standard deviation of multiple experiments.

3. Results and discussion

3.1. Particle size variation

Transmission electron microscopy images (Fig. 2a–c) show agglomerated CuO nanoparticles made in open FSP. They exhibit increasing primary particle diameter with increasing FSP-feed ratio, P/D. For the enclosed FSP the primary particle diameters increase substantially (Fig. 2d) compared to open FSP configuration (Fig. 2b) of equal P/D (5/5).

Consistent with these images, Fig. 3 shows the influence of the FSP-feed ratio (P/D-variation) on product CuO primary particle diameter. Here, the CuO particle diameter (d_{XRD}, squares and d_{BET}, circles) ranges from about 6 nm (d_{BET}) at P/D = 2/8 to about 17 nm (d_{BET}) at P/D = 7/3. The small particles (at low P/D), however, seem to be polycrystalline as d_{XRD} is clearly smaller than d_{BET}. Increasing the dispersion O_2 flow rate progressively shortens the flame and thus the particle's high temperature residence time for crystallization [19].
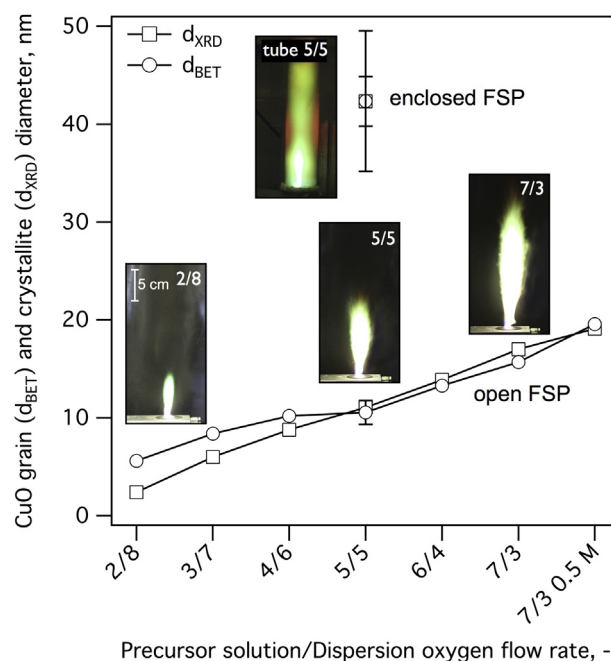

Fig. 3. Influence of combined precursor solution and dispersion oxygen flow rate variation on product CuO crystal size (d_{XRD}, squares) and BET equivalent diameter (d_{BET}, circles) in open, and enclosed FSP-configuration. The insets show photographs of the open FSP at P/D = 2/8, 5/5 and 7/3, as well as tube-enclosed FSP at P/D = 5/5.
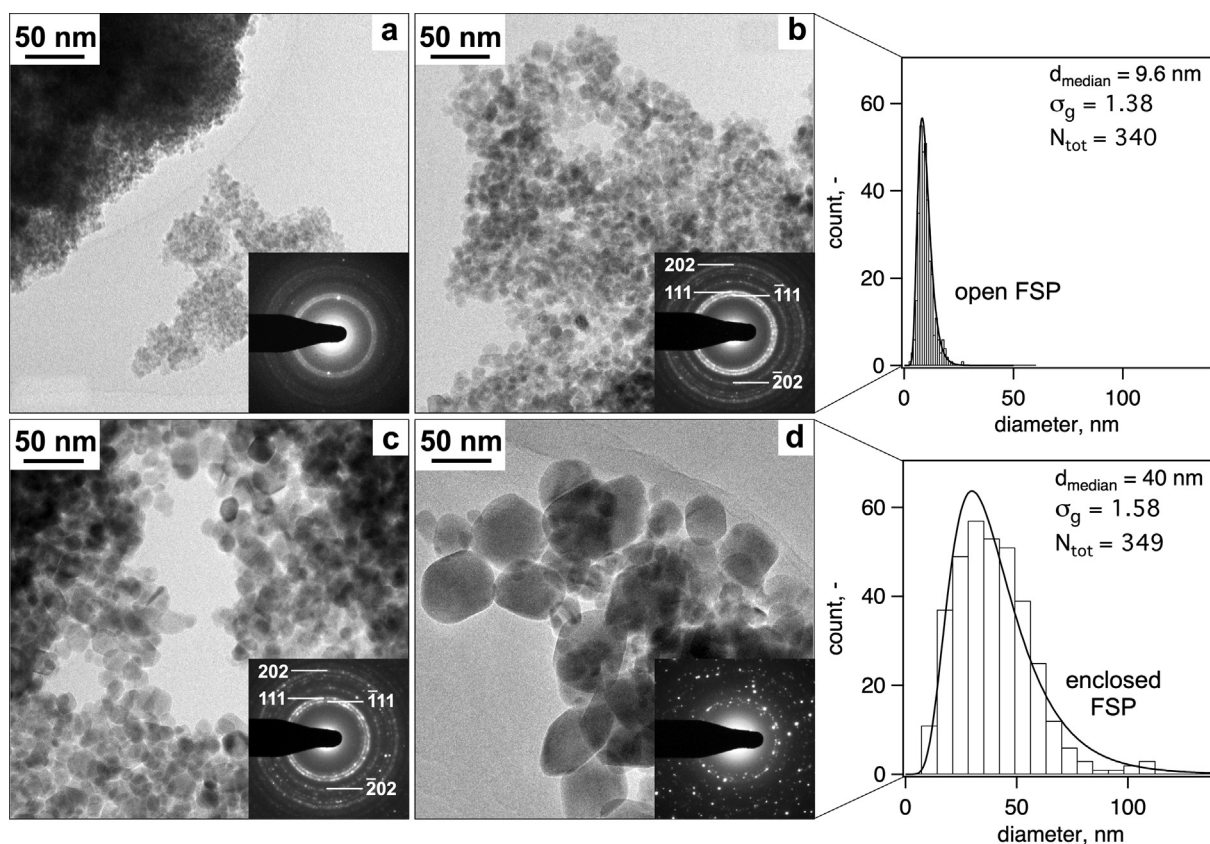

Fig. 2. TEM images and corresponding SAED spectra of CuO produced at various flame aerosol synthesis conditions: open FSP at precursor solution (P, ml min^{-1}) to dispersion O_2 (D, L min^{-1}) feed ratio, P/D = a) 2/8, b) 5/5, c) 7/3 and d) enclosed FSP at P/D = 5/5. Counted particle size distributions from open (b) and enclosed (d) FSP are nearly lognormally-shaped with geometric standard deviation (σ_g) of 1.38 and 1.58, respectively.

The underlying mechanism for size variation lies in the different temperature history of the particles [19] and droplet/particle concentration of the respective flames [15]. These factors are controlled by the FSPs settings (including precursor solution composition and burner configuration) [15]. For increasing dispersion O_2 flow rate, D, for example, the flame shortens as the mixing of spray-droplets and O_2 is intensified, accelerating droplet evaporation and combustion while the product aerosol is diluted [26]. Therefore, the high temperature particle residence time is reduced. Worth mentioning here is that the product aerosol is diluted by both the dispersion O_2 itself and the accompanying ambient air entrainment [27,28]. Both effects, short flame and dilution, lead to smaller particles as there is less time and lower probability that particles collide (reduced particle–particle collisions) and sinter to bigger ones. In contrast, the increase in precursor flow rate, P, results in longer flames of higher enthalpy content and higher precursor concentration, leading to increased high temperature particle residence time and more particle–particle collisions, resulting in larger particles by enhanced coagulation & sintering [19]. The P/D variation at constant precursor concentration of 0.25 M Cu leads to control of the product primary particle diameter (d_{BET}) from 6 to 17 nm. While at constant $P/D = 7/3$, doubling the precursor Cu molarity from 0.25 to 0.5 M Cu increases the primary particle diameter from 17 to 20 nm (d_{BET}). The individual influences of dispersion gas and precursor flow rates variation on CuO primary particle diameter in open FSP configuration is shown as Supplementary data (Figs. A1 and A2).

Enclosing the FSP unit with a quartz glass tube hinders ambient air entrainment [27,28] to the flame and increases drastically the primary particle diameter compared to the open FSP configuration (Fig. 3): For $P/D = 5/5$ and 0.25 M Cu the product d_{BET} increases from about 10 to 50 nm which can be attributed to prolonged particle exposure to elevated temperatures [29], leading to extended particle growth by sintering. It should be noted that particles made by enclosed FSP have also substantially wider size distribution (Fig. 2d: $\sigma_g = 1.58$) than those made by open FSP (Fig. 2b: $\sigma_g = 1.38$) indicating broader high temperature residence time, possibly arising from flow recirculation.

Fig. 4 shows X-ray diffraction patterns of CuO particles made at various FSP conditions (Fig. 3) in comparison to commercial CuO (Sigma Aldrich, CuO <5 μm, 98%). All show pure monoclinic CuO (Tenorite, ICSD 016025 or JCPDS 48-1548) with increasing peak broadening for decreasing P/D. This indicates a reduction in CuO crystal size according to Scherrer's equation [30] from 53 nm (commercial CuO) to 2.4 nm polycrystalline CuO particles made with the $P/D = 2/8$ flame.

3.2. Electrochemical performance

The flame-made CuO was tested for its electrochemical performance and compared to that of relatively large, commercial CuO particles of 670 nm (d_{BET}). Fig. 5a shows the potential (vs. Li/Li$^+$) as a function of specific charge (or composition, x) and the differential charge as a function of potential (Fig. 5b) for the first lithiation and delithiation cycles of electrodes containing CuO particles of $d_{BET} = 20$ (black solid line), 50 (red dashed line) and 670 nm (blue dotted line).

The onset of Li insertion into CuO can be observed at ∼2.25 V that is characterized by a sloping potential − specific charge profile (Fig. 5a) and small reduction peaks in the differential charge profiles (Fig. 5b) for the electrodes made with 20 and 50 nm CuO particles [31]. This insertion does not modify drastically the CuO structure but builds-up strain and corresponds well to the potential profile observed by Debart et al. [31]. Here, also the kinetics of insertion become evident as an extended sloping region for low
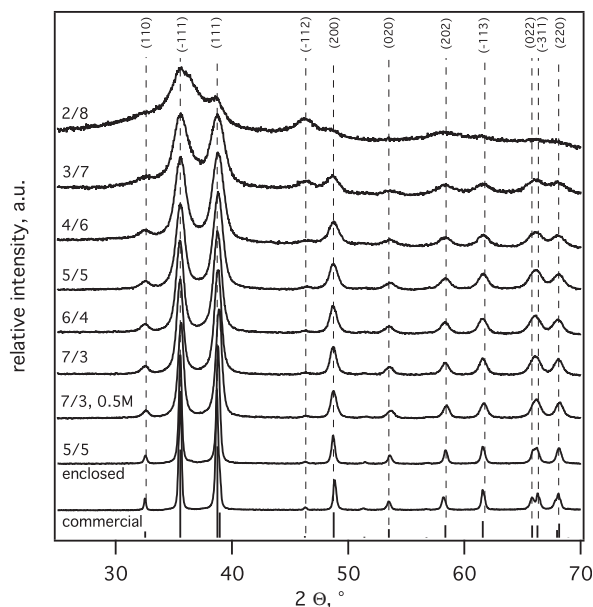

Fig. 4. X-ray diffraction patterns of as prepared CuO particles at various open FSP feed P/D and 0.25 M Cu (unless otherwise stated) in comparison to commercial CuO (Tenorite).

cycling rates of C/300 is observed by Debart et al. [31] compared to the faster cycling rates of C/5 used here.

An extended sloping potential region, however, is seen for the smaller CuO particles of 20 and 50 nm while no such feature is detected for the large 670 nm particles (Fig. 5a). This indicates a faster overall intercalation rate for the small starting CuO particles. The 670 nm particles even show a small potential dip around 1.3 V (Fig. 5a) and a corresponding sharp reduction peak in the differential charge spectra (Fig. 5b). Most likely this is caused by an activation process.

The plateau at about 1.3 V (Fig. 5a) and the corresponding differential charge peaks constitute the signature of the CuO conversion reaction (with intercalated Li) to Cu metal embedded in a Li$_2$O matrix. This reaction seems not to be affected by the starting CuO particle size as all potential profiles overlap. The small differential charge reduction peaks around 1.25 V for the 20 nm and even more pronounced for the 50 nm particles were not detected so far (to the best of our knowledge) and the origin of the background process remains yet unclear. However, for potentials below 0.8 V (Fig. 5a), the particle size dependent growth of a solid electrolyte interphase (SEI) layer becomes evident: Smaller particles (large SSA) encounter larger specific charges than larger particles (more charge consumption for the SEI layer formation due to the larger surface area in contact with the electrolyte).

Upon delithiation (oxidation), two characteristic plateaus are detected on the galvanostatic curves for the small starting CuO particles of 20 and 50 nm (d_{BET}). The first one around 2.35−2.4 V vs. Li/Li$^+$ for the oxidation of Cu^0 to Cu^I and the second one around 2.6 V for the oxidation of Cu^I to Cu^{II} [31]. The differential charge curve of the 670 nm particles, however, remains largely featureless, indicating inferior back-conversion (oxidation) during the initial cycles in agreement with the low specific charges in Fig. 6.

Fig. 6 shows representative electrochemical cycling results at C/5 rate. The electrode made with the 20 nm particles shows exceptionally high initial specific charge upon reduction, beyond 1050 mA h g^{-1} (Fig. 6, black solid line). Such high specific charge cannot come from CuO conversion alone as the maximal specific charge of that reaction is 674 mA h g^{-1} [32]. However, a fraction of
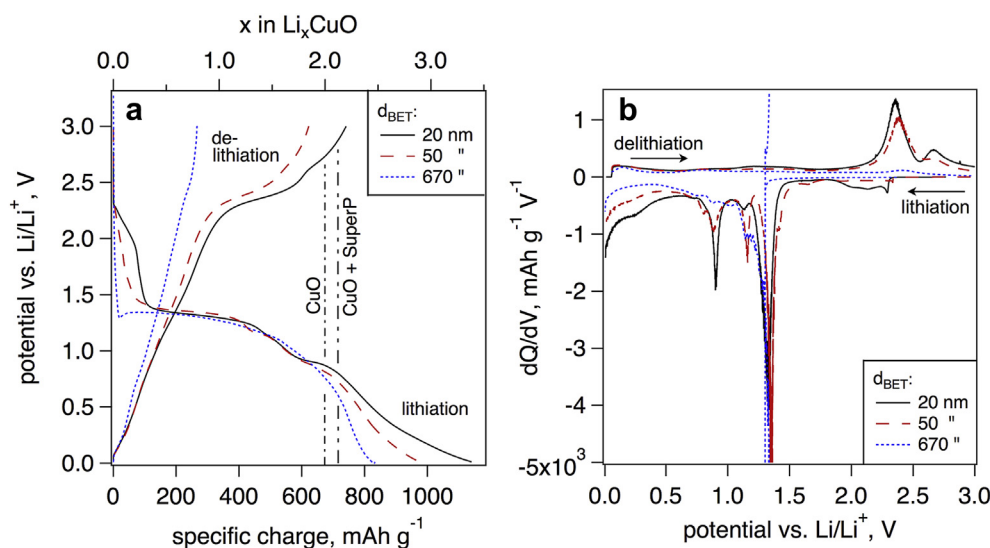
Fig. 5. a) Lithiation and delithiation potentials of the first cycle (vs. Li/Li$^+$) as a function of specific charge (or composition, x) and b) differential charges (dQ/dV) as a function of such potentials acquired at C/5 rate for FSP-made CuO of d_{BET} = 20 (black solid line) and 50 nm (red dashed line) and commercial CuO of d_{BET} = 670 nm (blue dotted line). The theoretical specific charge of CuO (dot-dashed line) as well as that accounting for the extra specific charge from SuperP carbon black (double-dot-dashed line) are also indicated. (For interpretation of the references to color in this figure legend, the reader is referred to the web version of this article.)

the additional specific charge during the first reduction can be attributed to formation of the SEI [33] around the electro-catalytically active Cu–Li$_2$O nano-grains [34], a process comprising charge transfer with alkyl carbonates of the electrolyte under Li uptake [35]. Another fraction of the charge also could come from pseudo-capacitive Li monolayer formation around the Cu–Li$_2$O grain boundaries at low potentials [36]. Furthermore, SuperP carbon black stores lithium in the respective potential window yielding about 600 mA h g^{-1} initial specific charge (including SEI formation) during the first lithiation and 285 mA h g^{-1} upon further cycling, as experimentally confirmed here and in good agreement with literature [7] (experiment not shown here). So by having 10 wt% SuperP in the electrode, about

86 mA h g^{-1} CuO (600*0.1/0.7) of the first discharge is due to the lithium intercalation in SuperP, and about 41 mA h g^{-1} CuO (285*0.1/0.7) of the following cycles has to be attributed to this reversible process.

Nevertheless, particle size dependence of the initial effects becomes evident, as with increasing CuO particle diameter the initial specific charge during discharge drops to about 823 mA h g^{-1} for the relatively large commercial 670 nm particles similar to nano Co$_3$O$_4$ [37]. After the first cycle, an increase in specific charge is observed for all three CuO sizes, indicating a conditioning of the electrode. This conditioning period (number of cycles) seems to scale with CuO size, such that for the commercial 670 nm CuO a steady increase in specific charge is seen over the investigated 130 cycles. This behavior indicates a size dependent activation of the CuO also seen for CoO as conversion reaction material [38].

After activation, the flame-made 20 nm CuO particles show specific charges in the order of 715 mA h g^{-1} – or 674 mA h g^{-1} after subtracting the equivalent 41 mA h g^{-1} of the SuperP inter-calation. So the theoretical specific charge of the conversion reaction (674 mA h g^{-1}) is reached. This high value, however, could not be maintained for more than a dozen cycles before rapid capacity fading starts. Smaller flame-made particles encounter even earlier fading, starting after only a few cycles for the 6 and 11 nm CuO (not shown). The mechanism of capacity fading is not clear; most plausible reasons are: a) exaggerated electrolyte degradation on the nano-sized particles by the increased metal-electrolyte contact area [13,39,40], b) loss of overall electrical conductivity through particle isolation [41] and c) increased charge transfer resistance [42]. All these effects become more pronounced as the specific surface area (SSA) and the number of grain boundaries increases with smaller particles. This is in line with the observation that the 50 nm CuO particles could maintain their still high specific charge (643/602 mA h g^{-1}, with/without SuperP equivalent) for about 50 cycles before capacity fading occurs and the relatively large 670 nm CuO sample even increases its specific charge to 530/489 mA h g^{-1} within the investigated 130 cycles (Fig. 6).

Consequently, coating the starting CuO particles (but keeping their electronic contact with the current collector) with a protective, yet Li-ion conductive SEI-type layer that would hinder direct particle–electrolyte contact could also hinder the pronounced
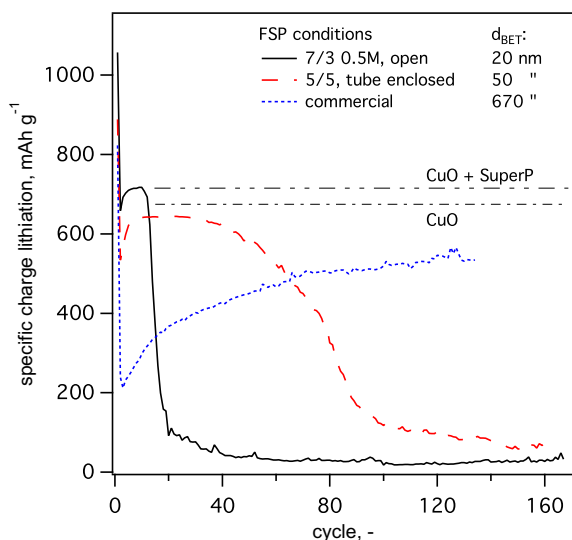
Fig. 6. Specific charge during lithiation of FSP-made CuO of d_{BET} = 20 (solid black line) and 50 nm (red dashed line) in comparison to commercial CuO having d_{BET} = 670 nm (blue dotted line) from galvanostatic cycling (C/5) between 3.0 and 0.01 V (vs. Li/Li$^+$). The theoretical specific charges of CuO (dot-dashed line) as well as that accounting for the extra specific charge from SuperP carbon black (double-dot-dashed line) are also shown. (For interpretation of the references to color in this figure legend, the reader is referred to the web version of this article.)

capacity fading due to possible electrolyte degradation and potentially also increase the interfacial charge transfer rate. Such coatings were successfully applied on intercalation-type cathode materials like $LiMn_2O_4$ [43], however, the feasibility of the concept would have to be tested for CuO. But then where does the higher specific charge of the smaller CuO starting material come from?

To shed light on the near theoretical specific charge, ex-situ XRD and XANES analyses of the electrochemically cycled material were made. Free-standing electrodes of 20, 50 and 670 nm CuO were cycled once (Fig. 7a,c) and 100 times (Fig. 7b,d) before encapsulation and analysis in delithiated (Fig. 7a,b) and lithiated states (Fig. 7c,d), showing specific charges comparable to Fig. 6.

On the one hand, the XRD patterns after the first complete cycle (delithiated state) in Fig. 7a show intensive metallic Cu (triangle) and minor Cu_2O (circles) Bragg reflexes for the large, 670 nm, CuO particles. On the other hand, the smaller, flame-made particles show minor metallic Cu but significant Cu_2O reflexes. This indicates superior back-conversion (oxidation) of the small particles upon initial delithiation compared to the relatively large, 670 nm particles.

After 100 cycles the XRD patterns for delithiated samples are inversed (Fig. 7b) as the small, 20 and 50 nm, starting CuO particles show intensive metallic Cu (triangle) and Li_2O (stars) reflexes. In contrast, the large, 670 nm, starting CuO particles show mainly Cu_2O and minor metallic Cu reflexes, in accordance with the increased specific charge shown in Fig. 6. All lithiated samples (Fig. 7c,d) show pure metallic Cu next to weak Li_2O reflexes irrespective of starting CuO size [13]. However, the XRD-derived Cu crystallite sizes from the (111) peak increase noticeably with cycle

number from about 2 nm after the first lithiation to about 5—6 nm after the 100th cycle, again independently of starting CuO size.

Similar metallic cluster sizes were observed for CuO [13] and also a size increase during cycling was seen for the CoO conversion reaction at a low cycling rate from about 2 to 4 nm within 5 cycles, stabilizing at 4 nm upon prolonged cycling [34]. Nevertheless, a direct correlation between Cu size increase and capacity fading is not plausible as the large 670 nm starting CuO still shows reasonable specific charge despite the larger Cu clusters (Fig. 6). Quantitative evaluation of the XRD data, however, was not possible as the grains tend to be very small, hence the Bragg reflexes are too broad for a meaningful de-convolution [13]. Instead, as the oxidation state of copper is one of the most interesting aspects regarding back-conversion, ex-situ Cu K-edge XANES analysis was investigated for the 50 and 670 nm samples after one cycle in delithiated state.

By performing a linear combination fitting of the electrode's Cu K-edge (Fig. 8) with the ones of reference materials (Cu, CuO and Cu_2O), the quantities of each component could be evaluated [44]. The relatively large 670 nm starting CuO particles contain about 74 wt% unreacted metallic Cu next to 24 wt% Cu_2O and some traces (2 wt%) of CuO. This is in line with XRD (Fig. 7) and also with XANES for similar sizes of starting CuO particles after the first charge [45]. In contrast, the flame-made starting CuO particles (d_{BET} = 50 nm) show significantly less Cu (22 wt%), about 42 wt% Cu_2O and 36 wt% CuO, hence a more complete oxidation during delithiation compared to the relatively large, 670 nm CuO starting particles.

The higher specific charge of nano-sized starting CuO (Fig. 6), in line with their more complete oxidation observed by XANES and XRD, suggests a benefit of nano-sized starting CuO for conversion
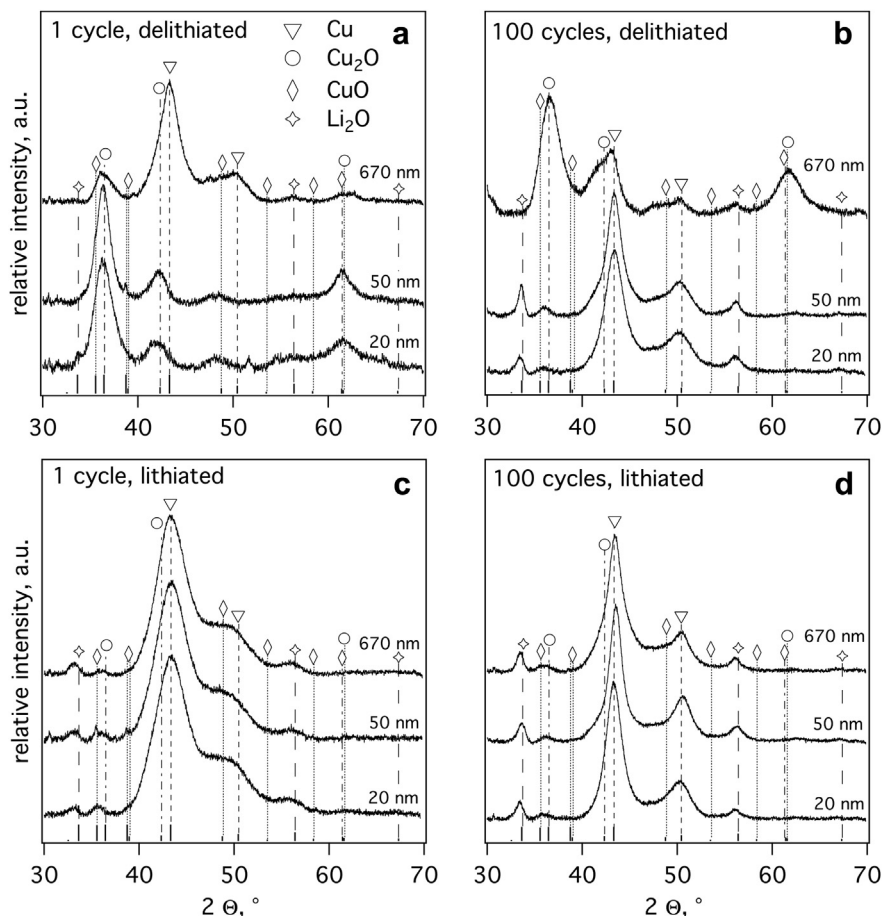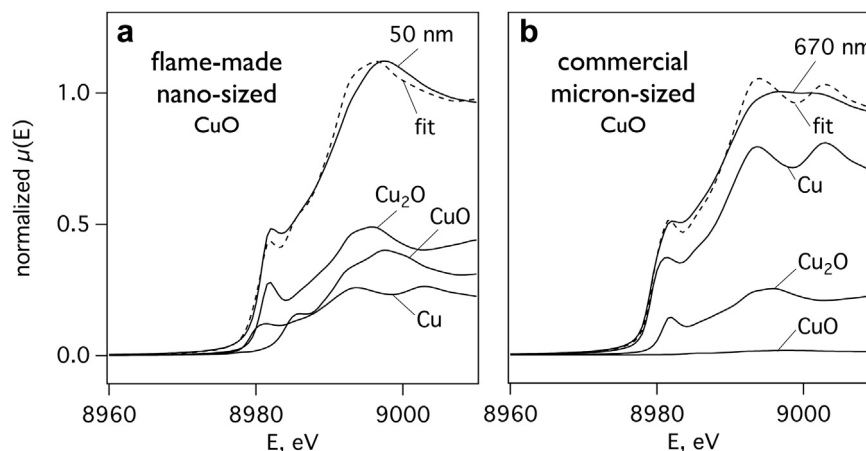

Fig. 7. X-ray diffraction patterns of free-standing electrodes (no Cu substrate) after electrochemical cycling between 0.01 V and 3.0 V at C/10 in delithiated state (a, b) and in lithiated state (c, d).

Fig. 8. Linear combination fitting (dashed line) of Cu-K-edge XANES spectra (solid lines) of free-standing electrodes (no Cu substrate foil) made of a) 50 and b) 670 nm Cu particles after one lithiation to 0.01 V and one delithiation to 3.0 V at C/10. The spectra of large starting (commercial) CuO (b) support the XRD data (Fig. 7) showing metallic Cu as a result of incomplete back-conversion during delithiation where the spectra of smaller (a) starting CuO show less Cu and mainly Cu_2O and CuO.

reactions. Higher specific charge for nano-sized starting CuO seems to be an intrinsic size effect widely accepted [12,41,46–51]. Bigger starting CuO particles restrict the conversion reaction between the Cu/Cu_2O couple [13,41,52]. Here, we could show the underlying effect — i.e. having more complete oxidation during delithiation if nano-sized starting CuO is used.

4. Conclusions

Pure and monocrystalline CuO nanoparticles were continuously produced (up to 17 g h^{-1}) by scalable flame spray pyrolysis (FSP) with a precise control over a particle size range from 6 to 50 nm (d_{BET}) by varying the FSP-feed ratio of precursor solution flow rate to dispersion oxygen flow rate (P/D-ratio) and tube enclosing.

FSP-made CuO particles of d_{BET} = 20 and 50 nm and commercially available 670 nm ones showed distinctly size-dependent electrochemical performance: The initial specific charge scales inversely with the CuO particle size yielding up to 1050 mA h g^{-1} for the 20 nm (d_{BET}) particles where larger (670 nm) particles show about 823 mA h g^{-1} supporting the obviously strong influence of CuO specific surface area on the extra charge of the initial cycle.

Upon cycling, the flame-made CuO nanoparticles show higher (near theoretical) specific charge of 674 mA h g^{-1} compared to the commercial particles of 200–500 mA h g^{-1}. This results from more re-oxidation of nano-sized CuO during delithiation as proved by ex-situ XRD and XANES measurements. The 2e$^-$ back conversion of Cu/Li_2O to CuO/Li is possible with nano-sized CuO particles while incomplete oxidation is seen for their sub-micron sized counterparts.

This opens the opportunity to harness the full theoretical specific charge of conversion reaction materials when one overcomes the enhanced aging rate of nano-sized starting CuO. Cycle stability decreases dramatically when using high specific surface area (SSA) nanoparticles, indicating a profound dependence of cycle life on the CuO SSA exposed to the electrolyte.

Acknowledgments

Appendix A. Supplementary data

Supplementary data related to this article can be found at http://dx.doi.org/10.1016/j.jpowsour.2013.04.147

References

[1] K. Mizushima, P.C. Jones, P.J. Wiseman, J.B. Goodenough, Mater. Res. Bull. 15 (1980) 783–789.
[2] M.M. Thackeray, P.J. Johnson, L.A. Depicciotto, P.G. Bruce, J.B. Goodenough, Mater. Res. Bull. 19 (1984) 179–187.
[3] T. Ohzuku, Y. Makimura, Chem. Lett. (2001) 642–643.
[4] A.K. Padhi, K.S. Nanjundaswamy, J.B. Goodenough, J. Electrochem. Soc. 144 (1997) 1188–1194.
[5] J. Cabana, L. Monconduit, D. Larcher, M.R. Palacin, Adv. Mater. 22 (2010) E170–E192.
[6] J.M. Tarascon, S. Grugeon, M. Morcrette, S. Laruelle, P. Rozier, P. Poizot, C. R. Chim. 8 (2005) 9–15.
[7] H. Li, P. Balaya, J. Maier, J. Electrochem. Soc. 151 (2004) A1878–A1885.
[8] P. Poizot, S. Laruelle, S. Grugeon, L. Dupont, J.M. Tarascon, Nature 407 (2000) 496–499.
[9] T. Li, X.P. Ai, H.X. Yang, J. Phys. Chem. C 115 (2011) 6167–6174.
[10] L. Taberna, S. Mitra, P. Poizot, P. Simon, J.M. Tarascon, Nat. Mater. 5 (2006) 567–573.
[11] V. Etacheri, R. Marom, R. Elazari, G. Salitra, D. Aurbach, Energy Environ. Sci. 4 (2011) 3243–3262.
[12] F.S. Ke, L. Huang, G.Z. Wei, L.J. Xue, J.T. Li, B. Zhang, S.R. Chen, X.Y. Fan, S.G. Sun, Electrochim. Acta 54 (2009) 5825–5829.
[13] S. Grugeon, S. Laruelle, R. Herrera-Urbina, L. Dupont, P. Poizot, J.M. Tarascon, J. Electrochem. Soc. 148 (2001) A285–A292.
[14] Z.Y. Wang, F.B. Su, S. Madhavi, X.W. Lou, Nanoscale 3 (2011) 1618–1623.
[15] R. Strobel, S.E. Pratsinis, J. Mater. Chem. 17 (2007) 4743–4756.
[16] F.O. Ernst, H.K. Kammler, A. Roessler, S.E. Pratsinis, W.J. Stark, J. Ufheil, P. Novák, Mater. Chem. Phys. 101 (2007) 372–378.
[17] T.J. Patey, R. Buchel, S.H. Ng, F. Krumeich, S.E. Pratsinis, P. Novák, J. Power Sources 189 (2009) 149–154.
[18] O. Waser, R. Buchel, A. Hintennach, P. Novák, S.E. Pratsinis, J. Aerosol. Sci. 42 (2011) 657–667.
[19] S.E. Pratsinis, Prog. Energy Combust. 24 (1998) 197–219.
[20] T.J. Patey, R. Buchel, M. Nakayama, P. Novák, Phys. Chem. Chem. Phys. 11 (2009) 3756–3761.
[21] L. Madler, H.K. Kammler, R. Mueller, S.E. Pratsinis, J. Aerosol. Sci. 33 (2002) 369–389.
[22] F.O. Ernst, R. Buechel, R. Strobel, S.E. Pratsinis, Chem. Mater. 20 (2008) 2117–2123.

[23] T. Rudin, K. Wegner, S.E. Pratsinis, J. Nanopart. Res. 13 (2011) 2715–2725.
[24] B. Ravel, M. Newville, J. Synchrotron Radiat. 12 (2005) 537–541.
[25] P. Novák, W. Scheifele, F. Joho, O. Haas, J. Electrochem. Soc. 142 (1995) 2544–2550.
[26] I. Glassman, R. Yetter, Combustion, fourth ed., Academic Press, San Diego, 2008.
[27] S.A. Macgregor, Int. J. Heat Fluid Flow 12 (1991) 279–283.
[28] M.C. Heine, L. Madler, R. Jossen, S.E. Pratsinis, Combust. Flame 144 (2006) 809–820.
[29] A. Teleki, S.E. Pratsinis, K. Kalyanasundaram, P.I. Gouma, Sens. Actuator B 119 (2006) 683–690.
[30] U. Holzwarth, N. Gibson, Nat. Nanotechnol. 6 (2011), 534.
[31] A. Débart, L. Dupont, P. Poizot, J.B. Leriche, J.M. Tarascon, J. Electrochem. Soc. 148 (2001) A1266–A1274.
[32] P. Novák, B. Klapste, P. Podhajecky, J. Power Sources 15 (1985) 101–108.
[33] E. Peled, J. Electrochem. Soc. 126 (1979) 2047–2051.
[34] S. Grugeon, S. Laruelle, L. Dupont, J.M. Tarascon, Solid State Sci. 5 (2003) 895–904.
[35] S. Laruelle, S. Grugeon, P. Poizot, M. Dolle, L. Dupont, J.M. Tarascon, J. Electrochem. Soc. 149 (2002) A627–A634.
[36] P. Balaya, H. Li, L. Kienle, J. Maier, Adv. Funct. Mater. 13 (2003) 621–625.
[37] A. Ponrouch, M.R. Palacin, J. Power Sources 212 (2012) 233–246.
[38] J.S. Do, C.H. Weng, J. Power Sources 146 (2005) 482–486.
[39] P. Poizot, S. Laruelle, S. Grugeon, L. Dupont, J.M. Tarascon, Ionics 6 (2000) 321–330.
[40] J.S. Bridel, S. Grugeon, S. Laruelle, J. Hassoun, P. Reale, B. Scrosati, J.M. Tarascon, J. Power Sources 195 (2010) 2036–2043.
[41] X.P. Gao, J.L. Bao, G.L. Pan, H.Y. Zhu, P.X. Huang, F. Wu, D.Y. Song, J. Phys. Chem. B 108 (2004) 5547–5551.
[42] J.G. Kang, Y.D. Ko, J.G. Park, D.W. Kim, Nanoscale Res. Lett. 3 (2008) 390–394.
[43] D. Arumugam, G.P. Kalaignan, J. Electroanal. Chem. 624 (2008) 197–204.
[44] A. Gaur, B.D. Shrivastava, S.K. Joshi, Copper K-edge XANES of Cu(I) and Cu(II) Oxide Mixtures, in: Proceedings of the 14th International Conference on X-ray Absorption Fine Structure (XAFS14) (2009).
[45] H.C. Choi, Y.M. Jung, S.B. Kim, Int. J. Nanosci. 1 (2002) 443–447.
[46] J. Morales, L. Sanchez, F. Martin, J.R. Ramos-Barrado, M. Sanchez, Electrochim. Acta 49 (2004) 4589–4597.
[47] X.H. Huang, C.B. Wang, S.Y. Zhang, F. Zhou, Electrochim. Acta 56 (2011) 6752–6756.
[48] J.Y. Xiang, J.P. Tu, Y.F. Yuan, X.L. Wang, X.H. Huang, Z.Y. Zeng, Electrochim. Acta 54 (2009) 1160–1165.
[49] J.C. Park, J. Kim, H. Kwon, H. Song, Adv. Mater. 21 (2009) 803–807.
[50] H.B. Wang, Q.M. Pan, J.W. Zhao, W.T. Chen, J. Alloys Compd. 476 (2009) 408–413.
[51] L.B. Chen, N. Lu, C.M. Xu, H.C. Yu, T.H. Wang, Electrochim. Acta 54 (2009) 4198–4201.
[52] D.W. Zhang, T.H. Yi, C.H. Chen, Nanotechnology 16 (2005) 2338–2341.